A Measurable Lawson Criterion and Hydro-Equivalent Curves for Inertial Confinement Fusion

Introduction

In inertial confinement fusion[1,2] (ICF), a shell of cryogenic deuterium and tritium ice is imploded at high velocities (~2 to 4×10^7 cm/s) and low entropy to achieve high central temperatures and high areal densities. The final fuel assembly consists of a relatively low density (~30 to 80 g/cc), high-temperature (~4 to 8 keV) core (the hot spot) surrounded by a dense (~300 to 1000 g/cc), cold (~100 eV) fuel layer (the compressed shell). The Lawson criterion[3] determining the onset of thermonuclear ignition is usually expressed through the product $p\tau > 10$ atm $\times$ s, where p is the plasma pressure in atm and τ is the energy confinement time in seconds. In magnetic fusion devices, both the pressure and confinement time are routinely measured, and the performance of each discharge can be assessed by comparing the value of $p\tau$ with respect to the ignition value (10 atm $\times$ s). In inertial confinement fusion, both p and τ cannot be directly measured and the performance of sub-ignited ICF implosions cannot be assessed with respect to the ignition condition. Often, the Lawson criterion is extended to ICF by simply restricting its application to the hot spot and by replacing p with the ideal gas equation of state $p = 2\rho_h T_h / m_i$ (ρ_h is the hot-spot mass density, T_h is the hot-spot temperature, and m_i is the DT average ion mass) and τ with the sound wave's traveling time through the hot spot, $t \sim R_h / C_s$ (here R_h is the hot-spot radius and C_s is the hot-spot sound speed, $C_s \sim \sqrt{T_h}$). This leads to the hot-spot–ignition condition $(\rho_h R_h)\sqrt{T_h} > $ const, where $\rho_h R_h$ is the hot-spot areal density. Such a simple derivation creates two problems: (a) the confinement time is incorrect since it neglects the inertial confinement of the surrounding cold shell, and (b) the hot-spot areal density cannot be experimentally measured.

A more accurate form of the hot-spot–ignition condition is given in Refs. 1 and 4–6 with the alpha heating balancing all the hot-spot power losses (thermal conduction and radiation losses). Our approach to ignition is somewhat different than the one in Ref. 4. First, our ignition model is dynamic since it includes both the compression and expansion phases of the shell motion. Second, our ignition condition is given in terms of the total areal density rather than the hot-spot areal density. Third, the ignition condition is viewed as an instability of both the pressure and the temperature rather than only the temperature. This causes the heat conduction losses to enter the ignition condition in a fundamentally different way. A more detailed discussion of this point is provided in the next section. It is important to emphasize that the presence of a cold, dense shell surrounding the hot spot significantly alters the onset of the thermonuclear instability (a similar point is made in Refs. 4, 7, and 8). Since the heat conductivity is negligible in the cold shell, most of the heat leaving the hot spot is recycled back into the hot spot in the form of internal energy and pdV work of the plasma ablated off the inner shell surface. Much of the radiation losses are also recycled back through ablation since the cold shell is opaque to the low-energy portion of the x-ray bremsstrahlung spectrum (only the high-energy x rays can penetrate the dense shell). As argued in Ref. 7, the heat conduction and, to some extent, the radiation losses do not appreciably change the hot-spot pressure (i.e., energy). Instead, those losses raise the density and lower the temperature while keeping $p \sim \rho T$ approximately constant. The fusion rate scales as $n^2 \langle \sigma v \rangle$, where n is the ion density and $\langle \sigma v \rangle$ is the fusion reactivity. Since $\langle \sigma v \rangle \sim T^{3-4}$ for $T < 6$ to 8 keV and $\langle \sigma v \rangle \sim T^2$ for 6 to $8 < T < 25$ keV, it follows that the alpha self-heating is degraded by heat conduction and radiation losses only at low temperatures less than 6 to 8 keV but unchanged at high temperatures $T > 6$ to 8 keV. This occurs because at high temperatures, the fusion rates depend only on the hot-spot pressure $(n^2 \langle \sigma v \rangle \sim p^2)$, which is independent of the heat losses. While these recycling effects (described in details in Ref. 7) improve the ignition threshold, the expansion losses, which are often not included in the ignition condition, causes a transfer of internal energy to kinetic energy and degrade the ignition conditions. Since hot-spot expansion occurs against the dense shell, the ignition conditions depend on the inertia of the dense shell. Furthermore, the hot spot's internal energy comes from the shell's kinetic energy, which is also used to assemble the shell's areal density. As shown in Ref. 9, there is a direct correlation between the hot spot areal density and the shell's areal density. Thus one can expect that the ICF Lawson criterion depends on the shell's areal density.

In this article, we derive a form of the Lawson criterion that can be directly measured in ICF implosions and includes the confinement of the surrounding cold shell. One can use such a new criterion to assess how far current and future sub-ignited ICF implosions are from achieving ignition. Such a new ignition criterion depends on the only two measurable quantities in the ICF fuel assembly: the total areal density and the hot-spot ion temperature. Note that the total areal density comes mostly from the cold shell surrounding the hot spot and is directly related to the inertial confinement time. In cryogenic implosions, the total areal density can be measured through charged-particle spectroscopy or x-ray radiography. The ion temperature is measured with neutron time-of-flight (nTOF) diagnostics.[10] For instance, recent cryogenic implosions[11] of D_2 targets on the OMEGA laser[12] have achieved a fusion burn–averaged areal density exceeding 200 mg/cm^2 and burn-averaged ion temperature of 2 keV—the highest performance for a cryogenic implosion to date. The burn-averaged areal density has been measured through the energy downshift of the proton spectrum from secondary $D + He^3$ reactions.[13] The ion temperature was measured through the nTOF diagnostics. The ion temperature used in the ignition condition is computed without alpha-particle heating. Thus, our measurable Lawson criterion is applicable to D_2 surrogate targets and DT sub-ignited implosions. Obviously, ignited DT implosions do not need a theoretical ignition criterion to verify that ignition conditions have been achieved.

We also show that hydro-equivalent curves can be represented on the same $\left(\rho R_{tot}, T_i^h\right)$ plane. Hydro-equivalent curves are defined as curves with constant adiabat and implosion velocity. Since the laser energy is the only parameter varying along such curves, they can be used to predict how a given implosion would perform when scaled up to a larger laser. For example, any implosion carried out on OMEGA[12] is represented by a point on a hydro-equivalent curve. By increasing the laser energy and keeping the implosion hydro-equivalent, the point on the diagram moves along the hydro-equivalent curve. If that point ends up within the ignition region for NIF-like energies, one can then conclude that particular OMEGA implosion scales to one-dimensional ignition on the National Ignition Facility (NIF).[14]

The remaining sections of this article (1) describe the analytic ignition model and derive its initial conditions; (2) derive the ignition condition from the analytic model and compare it with the results of one-dimensional hydrodynamic simulation; (3) discuss the assumptions concerning the alpha-particle confinement and compare with previous forms of ignition condition; and (4) derive the hydro-equivalent curves and discuss them in the conclusions.

Dynamic Model of Thermonuclear Ignition

The dynamic model described in this section includes standard energy losses and sources (heat conduction, radiation losses, alpha heating) as well as compression and expansion dynamics of a hot spot surrounded by a dense shell. The model describes the assembly phase of the hot spot up to ignition. It does not include the propagation of the burn wave or the disassembly of the ignited fuel. As such, energy gains are not calculated and the focus is restricted to the onset of thermonuclear instability in the hot spot (i.e., ignition).

In the derivation of ignition conditions, the hydrodynamic model of Refs. 7 and 8 is closely followed. During assembly of the hot spot, its temperature is high and the flow velocity is less than the hot spot's sound speed. Thus, the subsonic model of Refs. 7 and 8 is adopted and the kinetic energy with respect to the internal energy inside the hot spot is neglected. It is assumed that most of the alpha particles generated from the fusion reactions deposit their energy into the hot spot, requiring that the size of the hot spot exceeds the alpha particle's mean free path. This condition depends on the hot spot's areal density and temperature and is verified *a posteriori*. Energy losses in the hot spot include heat conduction and bremsstrahlung radiation. Conservation of the hot spot's energy including the *pdV* work of the shell, the alpha-particle heating, and the conduction and radiation energy losses, can be written in the following simple form:

$$\frac{\partial}{\partial t}\left(\frac{p}{\gamma-1}\right) + \nabla \times \left[\vec{u}\left(\frac{\gamma p}{\gamma-1}\right)\right] = \nabla \times \kappa(T)\nabla T$$
$$+ \frac{\theta\rho^2}{4m_i^2}\langle\sigma v\rangle\varepsilon_\alpha - \nabla \cdot \vec{F}, \quad (1)$$

where $\rho(r,t)$, $p(r,t)$, $\vec{u}(r,t)$ are the hot-spot density, pressure, and velocity, respectively. Here γ is the ratio of specific heats or adiabatic index ($\gamma = 5/3$) and $\kappa(T) = \kappa_0 T^\nu$ is the Spitzer thermal conductivity with $\nu = 5/2$. The second term on the right-hand side of Eq. (1) represents the alpha particle's energy deposition, with θ being the absorbed alpha-particle fraction depending on the hot spot's areal density and temperature, m_i the ion mass for DT, $\varepsilon_\alpha = 3.5$ MeV the alpha-particle energy from DT reactions, and $\langle\sigma v\rangle$ the fusion reaction rate as a function of the ion temperature T. The last term is the bremsstrahlung radiation. The radiation flux $\vec{F}$ is the first moment of the radiation field over angle[15] integrated over all frequencies. The radiation flux $\vec{F}$ depends on

both the bremsstrahlung radiation and absorption processes. The bremsstrahlung emission[1,16] for the hot-spot plasma is expressed in terms of its pressure and temperature as $j = C_1 p^2 T^{-3/2}$, where $C_1 \approx 3.88 \times 10^{-29} Z^3/(1 + Z)^2$ in m $\times$ J$^{5/2}$ $\times$ s^{-1} $\times$ N^{-2}, pressure p in N/m^2, temperature T in J, and j in W/m^3.

Inside the hot spot, the temperature is high and the plasma is optically thin. At the interface of the hot spot and the cold shell, the temperature drops significantly and much of the radiation energy escaping the hot spot is absorbed near the inner shell surface. The mean free path (l) of photons[1,16] with energy $h\nu$ in a DT plasma is

$$l \approx 2.25 \times 10^4 \frac{\sqrt{T}(h\nu)^3}{\rho^2}, \qquad (2)$$

where l is in μm, ρ is the plasma density in g/cm^3, T is the plasma temperature in keV, and $h\nu$ is in keV. Consider the free–free emission in a marginal's ignited hot spot of typical radius $\sim$50 μm, temperature 5 keV, and density $\sim$50 g/cm^3. Most of the radiation energy is carried by photons with energy below 5 keV. According to Eq. (2), the mean free path of 5-keV photons ($l \sim$ 2500 μm) is much longer than the size of the hot spot. Therefore, typical hot spots are transparent to bremsstrahlung radiation. On the contrary, a 5-keV photon has a very short mean free path in the cold shell surrounding the hot spot. For typical compressed shell densities of $\sim$600 g/cm^3 and temperatures of $\sim$200 eV, the mean free path of a 5-keV photon is only 3.5 μm, much shorter than the typical dense shell thickness of 50 μm. This shows that in the fuel assembly of typical ICF implosions, the hot spot is optically thin and the opacity increases sharply near the shell's inner surface, resulting in a narrow absorption zone with strong attenuation at the hot spot/shell interface.

For typical ICF plasmas near stagnation, the hot-spot temperature is high enough that its sound speed exceeds the flow velocity. The fuel assembly develops an isobaric configuration,[7,8,17] and the hot spot has a flat pressure profile with $p \approx p(t)$. The temperature of the high-density shell is much less than that of the low-density hot spot. By neglecting the radiation energy, a self-similar solution for the hot-spot temperature[7] is obtained as $T = T_0 \hat{T}(\hat{r})$, where T_0 is the central temperature in the hot spot and $\hat{r}$ is the radius r normalized to the hot-spot radius R_h as $\hat{r} = r/R_h$,

$$\hat{T} \approx (1 - \hat{r}^2)^{2/5}/(1 - 0.15\hat{r}^2).$$

This profile indicates $T(\hat{r} = 1) \to 0$ at the boundary between the hot spot and the shell. The radiation flux reaching the hot-spot boundary is

$$F(R_h) = \int_0^{R_h} jr^2 \,\mathrm{d}r = C_1 p^2 T_0^{-3/2} R_h^3 \int_0^1 \hat{T}^{-3/2} \hat{r}^2 \,\mathrm{d}\hat{r}.$$

This radiation flux is absorbed and recycled back into the hot spot with the ablated material at the shell's inner surface. As the heat conduction losses are also recycled back into the hot spot via the ablated shell material, both effects alter the hot-spot temperature's evolution without appreciably changing the pressure.

After integrating Eq. (1) from 0 to the hot-spot radius $R_h(t)$, the heat conduction and radiation terms vanish since, as stated above, most of the heat and radiation fluxes are absorbed near the shell's inner surface; thus, the volume integral of the energy in Eq. (1) yields

$$\frac{1}{2}\dot{p}R_h^3 + \frac{5}{2}pR_h^2 u(R_h,t) = \frac{p^2 R_h^3}{(1 + Z)^2}\int_0^1 \hat{r}^2 \frac{\theta \varepsilon_\alpha \langle \sigma v \rangle}{4T^2}\,\mathrm{d}\hat{r}, \quad (3)$$

where $\dot{p}$ is the time derivative of the pressure and $u(R_h,t)$ is the flow velocity at the shell's inner surface. The shell material is ablated into the hot spot as a result of the heat and radiation energy deposited at the shell's inner surface. The flow velocity resulting from the combination of the inner surface motion and the ablative flow is

$$u(R_h,t) = \dot{R}_h - V_a, \qquad (4)$$

where V_a is the ablation velocity and $\dot{R}_h$ scales with the implosion velocity. Since $V_a \ll \dot{R}_h$, the ablation velocity can be neglected and Eq. (3) can be rewritten as

$$\frac{\mathrm{d}}{\mathrm{d}t}(pR_h^3) + 2pR_h^2 \dot{R}_h = \frac{2p^2 R_h^3}{(1 - Z)^2} f(T). \qquad (5)$$

Notice that pR_h^3 is proportional to the total internal energy of the hot spot and $pR_h^2\dot{R}_h$ to the pdV work. The function $f(T)$, defined as $f(T) \equiv (\theta \varepsilon_\alpha/4)\int_0^1 \hat{r}^2 (\langle \sigma v \rangle/T^2)\mathrm{d}\hat{r}$ represents the alpha-particle heating with the fusion reactivity being a function of the temperature T. Observe that $f(T)$ is constant if $\langle \sigma v \rangle$ is approximated with a quadratic power-law dependence on the temperature.

Some of the points made here about the recycling of the heat-conduction losses into the hot spot were also highlighted in Refs. 7, 8, and 17. In Ref. 17, it was also argued that a similar effect applies to the alpha particles leaving the hot spot. That is, the alpha particles leaving the hot spot are efficiently stopped by the dense shell within a narrow layer, thus causing the dense shell material to ablate into the hot spot. The ablated material would recycle the alpha particle's energy back into the hot spot in the form of internal energy of the ablated material. As argued

in Ref. 17, similarly to the heat conduction, alpha-particle losses do not lead to a lower hot-spot energy (i.e., pressure) but only to a lower temperature. In this optimistic scenario, the parameter θ in Eq. (1) would be close to unity since all the alpha-particle energy is retained within the hot spot. In our model, we set $\theta \approx 1$ and verify *a posteriori* whether or not the hot spot's areal density is large enough to confine most of the alphas (see the **Alpha-Particle Confinement** section, p. 213).

To simplify the analysis, we use a simple numerical fit of $f(T)$ as a power of the temperature $f(T) = \left(\varepsilon_\alpha T_*^\sigma / 4c_k^2 + \sigma\right) C_0 \hat{T}^\sigma$ after integration over the hot-spot volume, where $c_k = 1.6 \times 10^{-16}$ J/keV, $\varepsilon_\alpha = 5.6 \times 10^{-13}$ J, $C_0 \approx 2.6 \times 10^{-26}$ m³ × keV⁻³ × s⁻¹ for $\sigma = 1$ and T_* in J is defined later in Eq. (8). A comparison between the numerical fit and the accurate values of the fusion-reaction rate from Ref. 18 is shown in Fig. 116.39 for temperatures in the range of 3 to 8 keV. It is important to notice that the fusion reactivity follows a T^3 power law for temperatures $3 < T < 8$ keV and a T^2 power law for $8 < T < 25$ keV. To accurately capture the onset of the thermonuclear instability, we use a T^3 fit that is more accurate near the ignition threshold temperatures below 8 keV. Using the power-law dependence of fusion reactivity also helps to define the onset of the ignition process. In the power-law model, the thermonuclear instability does not saturate since the fusion burn continues until the fuel is depleted. This causes the solution of the ignition model to develop an explosive instability or mathematical singularity. It follows
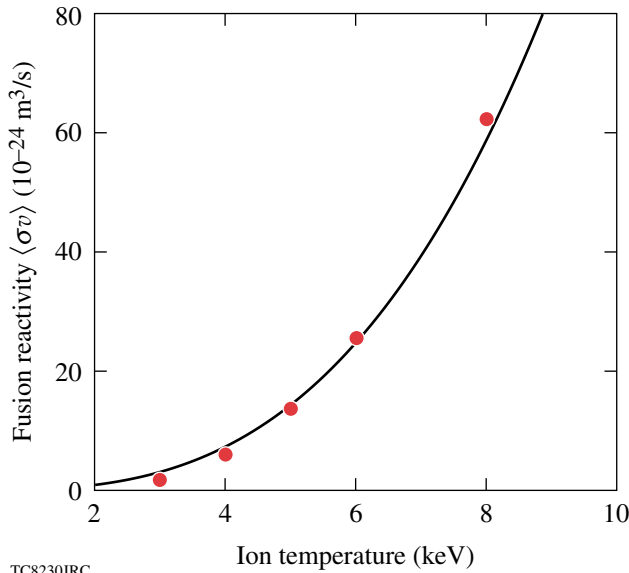

TC8230JRC

Figure 116.39
Fusion reactivity $\langle \sigma v \rangle$ is plotted as T^3 (solid curve). The dots are data taken from Ref. 18.

that one can identify the onset of ignition with the development of mathematical singularity. This can be easily explained by observing that in the absence of plasma motion $\left(\dot{R}_h = 0\right)$ and T^2 dependence of the reactivity, Eq. (5) reduces to

$$\frac{dp}{dt} = C_\alpha p^2,\qquad(6)$$

where the right-hand side represents alpha-particle heating and $C_\alpha > 0$. Equation (6) yields the explosive solution for $t > t_0$,

$$p(t) = \frac{p(t_0)}{1 - C_\alpha p(t_0)(t - t_0)}.\qquad(7)$$

If ignition occurs, our model develops an explosive solution even in the presence of energy losses. Equation (6) also helps to explain the difference in the heat-conduction treatment in Ref. 17 as compared to our model. Reference 17 makes the same argument made here (and in Ref. 7), that the heat conduction losses do not cause a net energy loss (p is not dependent on heat conduction) but do lead to a loss of temperature. Since in Ref. 17 ignition is defined as the condition for $dT/dt > 0$ [Eq. (26) of Ref. 17], the heat losses do enter into the ignition condition; however, the authors of Ref. 17 also realize that ignition can occur when $dT/dt < 0$. In this case, the temperature initially decreases but eventually reverses its course and increases rapidly. This form of ignition [which is not included in Eq. (26) of Ref. 17] can be included by defining ignition in terms of pressure increase ($dp/dt > 0$) rather than temperature increase ($dT/dt > 0$) as the pressure can increase even if the temperature decreases. Since our ignition model is dynamic, all the different paths to ignition are included with both pressure and temperature explosive growth.

It is useful to rewrite Eq. (5) in dimensionless form by defining the following normalization factors:

$$\tau = \frac{V_i t}{R_s}, \hat{p}(\tau) = \frac{p}{p_s}, \hat{R}(\tau) = \frac{R_h}{R_s},$$
$$\hat{T}(\tau) = \frac{T_0}{T_*}, T_* = \left(\frac{25\mu_1}{48\pi\kappa_0} p_s R_s V_i\right)^{2/7},\qquad(8)$$

where p_s and R_s are the hot-spot pressure and radius at stagnation and V_i is the implosion velocity. As will be shown in the **Solution of the Ignition Model and Marginal Ignition Condition** section (p. 209), T_* represents the stagnation temperature resulting from an adiabatic compression of the hot spot (in the absence of alpha heating and radiation losses). Here

T_* has the units of J with $\mu_1 \approx 0.55$ and $\kappa_0 = 3.7 \times 10^{69}$ m^{-1} × s^{-1} × J$^{-5/2}$ for $\ln\Lambda \approx 5$. For typical ICF implosion parameters, $T_*^{\text{keV}} \equiv T_*/c_k$ falls in the range of $5 \sim 8$ keV.

Using the power-law fit for $\langle \sigma v \rangle$ in Eq. (5) and substituting the dimensionless variables leads to the following simplified form of the energy equation:

$$\frac{d}{d\tau}\left(\hat{p}\hat{R}^5\right) = \gamma_\alpha \hat{p}^2 \hat{R}^5 \hat{T}^\sigma,\tag{9}$$

where $\gamma_\alpha = \left(\varepsilon_\alpha C_0 p_s R_s \big/ 2(1+Z)^2 c_k^{2+\sigma} V_i\right) T_*^\sigma$ is a parameter related to the initial shell condition at the beginning of the deceleration phase (see the **Initial Conditions** section, p. 209). Notice that Eq. (9) indicates that as long as the fusion reactivity $\langle \sigma v \rangle$ is proportional to $\sim T^2$ and the alpha heating rate depends only on the pressure ($n^2 \langle \sigma v \rangle \sim p^2$), the temperature does not enter into the ignition condition. This is not the case for $\langle \sigma v \rangle \sim T^{3-4}$ since the fusion-reaction rate will depend on pressure *and* temperature ($n^2 \langle \sigma v \rangle \sim p^2 T^{1-2}$). Here, an additional equation describing the evolution of the temperature is required.

Since the pressure is determined by the *pdV* work and the alpha-particle heating, one can use mass conservation and the equation of state to evaluate the temperature. The evolution of the hot-spot density depends on the mass ablation rate off the shell. This was first calculated in Refs. 7 and 8 and later in Ref. 19. The ablation rate can be determined by integrating the energy in Eq. (1) across the hot-spot boundary. All divergent-free terms vanish as both temperature and radiation flux approach zero at the hot-spot boundary. A straightforward integration leads to

$$\frac{5}{2A}\dot{m}_a T_0 R_h^2 = \frac{6}{5}\kappa_0 T_0^{\nu+1} R_h + \mu_0 C_1 p^2 T_0^{-3/2} R_h^3,\tag{10}$$

where the ablative mass rate is $\dot{m}_a = \rho V_a = Ap V_a/T$, $A = m_i/(1+Z)$, and $\mu_0 = \int_0^1 \hat{r}^2 \hat{T}^{-3/2} d\hat{r} \approx 0.85$. Notice that Eq. (10) is derived by approximating the temperature profile with a step function, the correct limit of a $\nu \gg 1$ expansion. Equation (10), accurate to order $1/\nu$, describes the energy flux balance at the hot-spot boundary where the radiation and conduction energy flows are recycled back by the ablated material.

The total hot-spot mass can be expressed as

$$M_{\text{hs}} = \int_0^{R_h} 4\pi \rho r^2 dr = 4\pi \mu_1 Ap R_h^3 \big/ T_0,$$

where $\mu_1 \approx 0.55$ is the value of the integral $\mu_1 = \int_0^1 \hat{r}^2/\hat{T} d\hat{r}$ and T_0 is the hot spot's central temperature. Due to mass conservation, the change of the hot spot's mass is caused by mass abla-

tion off the shell, $dM_{\text{hs}}/dt = 4\pi R_h^2 \dot{m}_a$. Substituting the above results into Eq. (10) yields

$$\frac{d}{dt}\left(\frac{pR_h^3}{T_0}\right) = \frac{12\kappa_0}{25\mu_1} R_h T_0^{5/2} + \frac{2\mu_0 C_1}{5\mu_1} \frac{p^2 R_h^3}{T_0^{5/2}}.\tag{11}$$

Notice that this equation governs the hot-spot temperature. Terms on the right-hand side represent heat conduction and radiation effects on the hot-spot temperature.

After a straightforward manipulation, the dimensionless form of the temperature equation can be written as

$$\frac{d}{d\tau}\left(\frac{\hat{p}\hat{R}^3}{\hat{T}}\right) = \hat{R}\hat{T}^{5/2} + \beta \frac{\hat{p}^2 \hat{R}^3}{\hat{T}^{5/2}},\tag{12}$$

where $\beta = 2\mu_0 C_1 p_s^2 T_*^{-3/2} R_s \big/ 5\mu_1 p_s V_i$. Notice that β is proportional to the ratio between the total radiation energy emitted from the hot spot and the imploding shell's kinetic energy. The radiation energy is proportional to $C_1 p_s^2 T_s^{-3/2} R_s^3 \tau_c$ and the shell's kinetic energy is proportional to the hot spot's internal energy $MV_i^2 \sim p_s R_s^3$. As shown below, the time $\tau_c \sim R_s/V_i$ represents the confinement time of the hot spot surrounded by a dense shell imploded with velocity V_i. Ignited ICF capsules require that the radiation energy be smaller than the compression work so that high temperatures can be reached in the hot spot. Furthermore, the bremsstrahlung losses are also smaller than the heat-conduction losses and do not appreciably alter the temperature profile, which is determined mostly by heat conduction.

The third and last equation of our ignition model governs the conservation of momentum of the thin shell surrounding the hot spot. The thin-shell approximation (discussed in Ref. 7) assumes that the entire shell kinetic energy is transferred to the internal energy of the hot spot upon stagnation. Even though the thin-shell model overestimates the stagnation energy, it yields the correct ignition scaling. This is shown in Ref. 8 where a more accurate shell model, the so-called "thick-shell" model, is compared with the "thin-shell" one. In the thick-shell model, the shell is treated as a finite-thickness, compressible gas, including the presence of a return shock driven by the rapid increase of the hot-spot pressure. A similar model was also later adopted in Ref. 19. While the thick shell is a more realistic (but more complicated) model than the thin-shell one, the ignition scaling is virtually the same. Furthermore, we will use the results of Refs. 9 and 20 to heuristically limit the transfer of kinetic energy from the shell to the hot spot, which, in the

thin-shell model, is overestimated (100% transfer). Within the frame of the thin-shell model, the shell compresses the hot spot like a spherical piston and the equation of motion for the shell is simply the shell Newton's law $M_s \ddot{R} = 4\pi p R^2$. In dimensionless form, this equation can be rewritten using Eq. (8) as

$$\frac{d^2 \hat{R}}{d\tau^2} = \hat{p} \hat{R}^2. \tag{13}$$

The shell Newton's law shows that the shell confinement time at stagnation scales as $\tau_c \sim \sqrt{M_s / p_s R_s}$. Since $M_s V_i^2 \sim p_s R_s^3$, the confinement time can be rewritten as $\tau_c \sim R_s / V_i$. During this time the hot spot's hydrodynamic pressure is at its peak value (in the absence of alpha heating). The shell's confinement time should not be confused with the burn time that depends on the shell's areal density (Ref. 1).

Equations (9), (12), and (13) represent a dynamic model of thermonuclear ignition. The next step is to determine the relevant set of initial conditions for the system of equations.

Initial Conditions

Based on the definition of the dimensionless variables, the initial condition of the thin-shell model requires that $\hat{R}(0) = R(0)/R_s$, $\dot{\hat{R}}(0) = -1$, $\hat{p}(0) = p(0)/p_s$, and $\hat{T}(0) = T_0(0)/T_*$, where $R(0)$, $p(0)$, $T_0(0)$ are the values of the radius, pressure, and central temperature at the beginning of the deceleration phase ($\tau = 0$) when the shell is imploding inward with its maximum velocity [$dR/dt(0) = -V_i$]. The stagnation values R_s and p_s can be defined through the energy conservation and adiabatic compression in the absence of alpha heating and radiation losses. In this case, energy conservation requires that $(1/2)M_s V_i^2 = (4\pi/3)p_s R_s^3$, while adiabatic compression requires that $p_s V_s^{5/3} = p(0)V(0)^{5/3}$ or $p_s R_s^5 = p(0)R(0)^5$. Using these relations, the initial conditions for the dimensionless variables can be rewritten as $\hat{R}(0) = \varepsilon_0^{-1/2}$, $\dot{\hat{R}}(0) = -1$, and $\hat{p}(0) = \varepsilon_0^{-5/2}$, where $\varepsilon_0 \equiv (1/2)M_s V_i^2 / (4\pi/3)p(0)R(0)^3$ is the ratio between the shell's kinetic energy and the hot spot's internal energy at the beginning of the deceleration phase. Notice that $\varepsilon_0 \gg 1$ in typical ICF implosions where the hot spot's energy is amplified many times during the deceleration of the shell. The initial condition for the temperature requires a special treatment. We start by integrating in Eq. (12) from the beginning of the deceleration phase ($\tau = 0$) to stagnation (τ_s). The stagnation values for the dimensionless variables are $\tau_s = \varepsilon_0^{1/2}$, $\hat{p}(\tau_s) = 1, \hat{R}(\tau_s) = 1$, and $\hat{T}(\tau_s) = 1$. The initial temperature $\hat{T}(0)$ can be inferred from an analysis of the temperature in Eq. (12). At the beginning of the deceleration phase, both pressure and temperature are small and the radiation losses can be neglected

with respect to heat losses. Neglecting the alpha-particle heating during the hot-spot assembly phase (that is, $\gamma_\alpha = 0$) results in the adiabatic compression of the hot spot, leading to $\hat{p}\hat{R}^5 = 1$. Thus, the temperature defined in Eq. (12) can be rewritten as

$$\frac{d\hat{\phi}}{d\tau} = \hat{\phi}^{-5/2} \hat{R}^{-4}, \tag{14}$$

where $\hat{\phi} \equiv \hat{p} \hat{R}^3 / \hat{T}$. The solution of Eq. (14) is

$$\hat{\phi}(\tau)^{7/2} = \hat{\phi}(0)^{7/2} + (7/2) \int_0^\tau \hat{R}^{-4} d\tau.$$

For large $\varepsilon_0 \gg 1$, one expects the stagnation temperature to be independent of its value at the beginning of the deceleration phase (as long as the initial value is much smaller than the stagnation value). Thus, one requires that $I \equiv (7/2) \int_0^\tau \hat{R}^{-4} d\tau \gg \hat{\phi}(0)^{7/2}$. Defining $\dot{\hat{R}} = d\hat{R}/d\tau$, the integral I can be rewritten as $I = (7/2) \int_0^\infty \hat{R}^{-4} \dot{\hat{R}}^{-1} d\hat{R}$. Notice that most of the contribution to the integral I comes from the stagnation values $\hat{R} \approx \hat{R}(\tau_s) = 1$ and $\dot{\hat{R}} \approx \dot{\hat{R}}(\tau_s) \approx 0$. By using the shell Newton's law [Eq. (13)], one finds that $\ddot{\hat{R}}(\tau_s) \approx 1$ and the shell velocity $\dot{\hat{R}}$ can be approximated by $\dot{\hat{R}} \approx \sqrt{2(\hat{R}-1)}$ near stagnation. Substituting into I and integrating over $\hat{R}$ yields $I = (5\pi/16\sqrt{2})$. At the beginning of the deceleration phase, the initial value of $\hat{\phi}$ is $\hat{\phi}(0) = \hat{p}(0)\hat{R}(0)^3 / \hat{T}(0) = [\varepsilon_0 \hat{T}(0)]^{-1}$. To guarantee a stagnation temperature independent of its initial value, one needs to choose $\varepsilon_0^{-1} \ll \hat{T}(0) \ll 1$. Any value of $\hat{T}(0) = \varepsilon_0^\omega$ with $-1 < \omega < 0$ satisfies this condition, and the resulting solution of the ignition model is independent of ε_0 and ω as long as $\varepsilon_0 \to \infty$. Here we choose $\omega = 1/2$ and $\hat{T}(0) = \varepsilon_0^{-1/2} \ll 1$.

Solution of the Ignition Model and Marginal Ignition Condition

Our ignition model consists of the three equations [(9), (12), and (13)] representing mass, momentum, and energy conservation, with the initial conditions derived in the **Initial Conditions** section (p. 209). For convenience, the equations and initial conditions are summarized below:

$$\frac{d}{d\tau}\left(\hat{p}\hat{R}^5\right) = \gamma_\alpha \hat{p}^2 \hat{R}^5 T^\sigma$$

$$\frac{d}{d\tau}\left(\frac{\hat{p}\hat{R}^3}{\hat{T}}\right) = \hat{R}\hat{T}^{5/2} + \beta \frac{\hat{p}^2 \hat{R}^3}{\hat{T}^{5/2}}$$

$$\frac{d^2 \hat{R}}{d\tau^2} = \hat{p}\hat{R}^2 \tag{15}$$

$$\hat{p}(0) = \varepsilon_0^{-5/2}, \hat{T}(0) = \varepsilon_0^{-1/2}, \hat{R}(0) = \varepsilon_0^{1/2}, \dot{\hat{R}}(0) = -1.$$

Equations (15) are numerically solved up to the stagnation time $\tau \sim \tau_s = \varepsilon_0^{1/2}$ for a large value of $\varepsilon_0 \gg 1$, and $\sigma = 1$ is used in the computation. The solution develops an explosive instability when the parameter γ_α exceeds a critical value for a preset value of β. Here, we are interested in the asymptotic value of γ_α for $\varepsilon_0 \to \infty$ (we use $\varepsilon_0 = 10^4$ in the numerical integration). Physically, this instability corresponds to the onset of ignition. The critical values of γ_α and β are obtained through a series of numerical solutions of the system of Eqs. (15) and shown in Fig. 116.40, where each dot represents a single pair of γ_α and β such that the solution of the equations turns singular for both pressure and temperature. The ignition curve in Fig. 116.40 can be accurately fitted by the following simple formula:

$$\gamma_\alpha = 1.12 + \beta^2 + 0.28\beta^3. \tag{16}$$

Within the frame of the thin-shell model, the shell thickness is negligible. The effects of finite thickness can be included, however, by noticing that only a fraction of the shell's kinetic energy is converted into hot-spot internal energy. That fraction is related to the ratio of the hot spot and shell volume at stagnation and can be written as $(1 + A^{-1})^{-3}$, where A is the aspect ratio defined as the hot-spot radius R_h over the shell thickness Δ, $A = R_h/\Delta$. The total mass is expressed as $M = 4\pi(\rho\Delta)R_s^2\Sigma(A)$ (Ref. 20) with the volume factor Σ defined as $\Sigma(x) = 1 + (1/x) + 1/(3x^2)$.
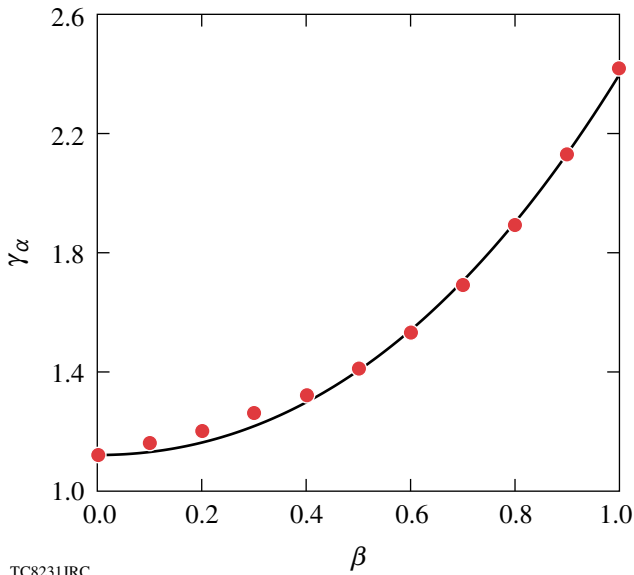

2.6

γ_α

1.8

1.4

1.0
0.0   0.2   0.4   0.6   0.8   1.0
β

TC8231JRC

Figure 116.40
Relation between γ_α and β. Each dot represents a single pair of γ_α and β such that the solution of Eqs. (15) turns singular. The solid curve is the fitting formula $\gamma_\alpha(\beta)$ in Eq. (16).

Thus, the important parameter γ_α in the ignition condition can be rewritten as

$$\gamma_\alpha = \frac{\varepsilon_\alpha C_0 T_*^\sigma}{2(1+Z)^2 c_k^{2+\sigma}} \frac{\sqrt{M}\sqrt{MV_i^2/(1+A^{-1})^3}}{4\pi R_s^2}$$

$$= \frac{\varepsilon_\alpha C_0 T_*^\sigma}{2(1+Z)^2 c_k^{2+\sigma}} \frac{\Sigma(A)}{(1+A^{-1})^{3/2}} (\rho\Delta)V_i. \tag{17}$$

Similarly, the temperature normalization factor T_* can be written as

$$T_* = \left(\frac{25\mu_1}{48\pi\kappa_0} \times \frac{M_s V_i^3}{R_s^2}\right)^{2/7}$$

$$= \left(\frac{25\mu_1}{12\kappa_0} \times \frac{\Sigma(A)(\rho\Delta)V_i^3}{(1+A^{-1})^{9/2}}\right)^{2/7}. \tag{18}$$

For typical ICF implosions, the stagnation aspect ratio A usually falls within the range of $1 < A < 4$ (Ref. 20). Within this interval, the function $\Sigma(A)/(1+A^{-1})^{9/2}$ can be approximated by the power law, $\Sigma(A)/(1+A^{-1})^{9/2} \approx 0.12A^{1.045}$. Since the stagnation aspect ratio scales with the implosion velocity and shell adiabat as $A \approx 8.2 \times 10^{-6} V_i^{0.96}/\alpha^{0.19}$ (Ref. 9), the function $\Sigma(A)$ can be approximated as

$$\Sigma(A)/(1+A^{-1})^{9/2} \approx \delta_0 V_i/\alpha^{0.2},$$

with the constant $\delta_0 = 5.7 \times 10^{-7}$ s/m. Substituting into Eq. (18) and solving for the implosion velocity yields

$$V_i = \left(\frac{12\kappa_0}{25\mu_1\delta_0}\right)^{1/4} \alpha^{0.05}(\rho\Delta)^{-1/4}T_*^{7/8}. \tag{19}$$

Notice that the adiabat dependence is very weak, so it is neglected in the following derivation. Furthermore, the aspect ratio's dependence in Eq. (17) can be approximated with a constant, $\Sigma(A)/(1+A^{-1})^{3/2} \approx 0.85$ for $1 < A < 4$. Substituting this result and Eq. (19) into Eq. (17), one finds the γ_α dependence on the areal density $\rho\Delta$ and temperature T_*:

$$\gamma_\alpha = \frac{0.85\varepsilon_\alpha C_0}{2(1+Z)^2 c_k^{2+\sigma}}\left(\frac{12\kappa_0}{25\mu_1\delta_0}\right)^{1/4}(\rho\Delta)^{3/4}T_*^{\sigma+7/8}. \tag{20}$$

The parameter β can be expanded in the same manner as above. Notice that $\beta/\gamma_\alpha \sim T_*^{-\sigma-3/2}$ and β can be written in the following form:

$$\beta = \frac{0.34\,\mu_0 C_1}{\mu_1}\left(\frac{12\kappa_0}{25\,\mu_1\delta_0}\right)^{1/4}(\rho\Delta)^{3/4}T_*^{-5/8}. \tag{21}$$

In both Eqs. (20) and (21), the units of $\rho\Delta$ and T_* are in kg/m^2 and J, respectively. To express T_* in keV in these equations, γ_α and β can be rewritten as

$$\gamma_\alpha = C_3(\rho\Delta)^{3/4}\left(T_*^{\mathrm{keV}}\right)^{15/8},$$

$$C_3 = \frac{0.85\varepsilon_\alpha C_0}{2(1+Z)^2 c_k^{9/8}}\left(\frac{12\kappa_0}{25\,\mu_1\delta_0}\right)^{1/4},$$

$$\tag{22}$$

$$\beta = C_4(\rho\Delta)^{3/4}\left(T_*^{\mathrm{keV}}\right)^{-5/8},$$

$$C_4 = \frac{0.34\,\mu_0 C_1}{\mu_1 c_k^{5/8}}\left(\frac{12\kappa_0}{25\,\mu_1\delta_0}\right)^{1/4},$$

where $Z = 1$ for DT plasma, $\varepsilon_\alpha = 3500$, $c_k = 5.6\times10^{-13}$ J, $C_0 = 2.6\times10^{-26}$ m$^3\times$keV$^{-3}\times$s^{-1}, $\mu_0 = 0.85$, $\mu_1 = 0.55$, $\kappa_0 = 3.7\times1069$ m$^{-1}\times$s$^{-1}\times$J$^{-5/2}$, $\delta_0 = 5.7\times10^{-7}$ m$^{-1}\times$s. Using $C_1 = 9.7\times10^{-30}$ m$\times$J$^{5/2}\times$s$^{-1}\times$N^{-2} for $Z = 1$ leads to $C_4 \approx 0.327$ keV$^{5/8}$ m$^{3/2}\times$kg$^{-3/4}$, and the parameter $\beta \leq 1$ for typical values of areal density and temperature. Using $C_0 \approx 2.6\times10^{-26}$ m$^3\times$keV$^{-3}\times$s^{-1} into the first equation of (22) yields $C_3 \approx 7.6\times10^{-3}$ keV$^{-15/8}\times$m$^{3/2}\times$kg$^{-3/4}$ for DT fuel.

The next step is to relate the parameter T^* to the maximum temperature in the absence of alpha heating $\left(T_{\max}^{\mathrm{no}\,\alpha}\right)$. Such a temperature is approximately equal to the temperature measured in D$_2$ targets or sub-ignited DT implosions where the self-heating plays a negligible role in the hot-spot energy balance. A more detailed discussion of the validity of $T_{\max}^{\mathrm{no}\,\alpha}$ as a measurable parameter is included in the **Conclusions** (p. 216). The value of $T_{\max}^{\mathrm{no}\,\alpha}$ is found by setting $\gamma_\alpha = 0$ and by solving Eq. (15) for various values of β. The maximum of the solution for $\hat{T}$ corresponds to $T_{\max}^{\mathrm{no}\,\alpha}/T_*$. A series of numerical solutions lead to the following relations between the parameter β and the maximum hot-spot temperature $\hat{T}_{\max}^{\mathrm{no}\,\alpha}$ without alpha heating:

$$\hat{T}_{\max}^{\mathrm{no}\,\alpha} = \frac{T_{\max}^{\mathrm{no}\,\alpha}}{T_*} = \frac{0.78}{\Pi(\beta)}, \tag{23}$$

$$\Pi(\beta) = 1 + 0.42\beta^{0.9} + 1.7\times10^{-3}\beta^{1.8},$$

as shown in Fig. 116.41. Using Eq. (23) and the definitions of γ_α and β in Eqs. (22), one can easily rewrite the ignition condition as

$$(\rho\Delta)\left(T_{\max}^{\mathrm{no}\,\alpha}\right)^{5/2} = 33.5\,\frac{\left[\gamma_\alpha(\beta)\right]^{4/3}}{\Pi(\beta)^{5/2}}, \tag{24}$$

where $\rho\Delta$ is in g/cm^2, $T_{\max}^{\mathrm{no}\,\alpha}$ is in keV, γ_α is given in Eq. (16), and β can be determined in terms of $T_{\max}^{\mathrm{no}\,\alpha}$ from the following equation:

$$\frac{\beta\Pi(\beta)^{5/2}}{\lambda_\alpha(\beta)}\left[\frac{3.4}{T_{\max}^{\mathrm{no}\,\alpha}}\right]^{5/2}. \tag{25}$$

Notice that for large temperatures $T_{\max}^{\mathrm{no}\,\alpha} \gg 3.4$ keV, β is small and the ignition condition reduces to

$$(\rho\Delta)\left(T_{\max}^{\mathrm{no}\,\alpha}\right)^{5/2} = 33.5\,\mathrm{g}\big/\mathrm{cm}^2\mathrm{keV}^{2.5}.$$

Numerically solving Eq. (25) for various $T_{\max}^{\mathrm{no}\,\alpha}$ in the range $2.5 < T_{\max}^{\mathrm{no}\,\alpha} < 8$ keV to find β and substituting $\beta\left(T_{\max}^{\mathrm{no}\,\alpha}\right)$ into

TC8232JRC

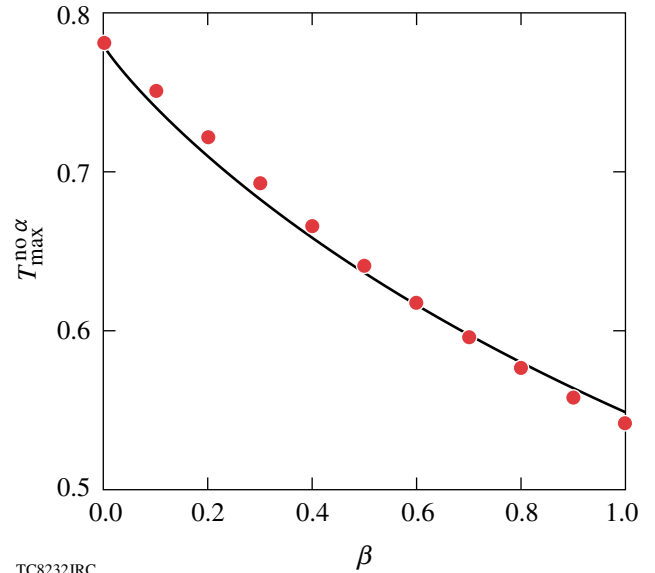Figure 116.41
Relation between $\hat{T}_{\max}^{\mathrm{no}\,\alpha}$ and β. Each dot represents a single pair of $\hat{T}_{\max}^{\mathrm{no}\,\alpha}$ and β by solving Eqs. (15) with $\gamma_\alpha = 0$ for various β. $\hat{T}_{\max}^{\mathrm{no}\,\alpha}$ is the maximum value of $\hat{T}$ in the solution. The solid curve is the fitting formula $\hat{T}_{\max}^{\mathrm{no}\,\alpha}(\beta)$ in Eq. (23).

Eq. (24) yields the ignition condition in terms of the two measurable parameters $\rho\Delta$ and $T_{max}^{no\,\alpha}$. Figure 116.42 shows the ignition condition in the $\rho\Delta$, $T_{max}^{no\,\alpha}$ plane. A simple fit of the ignition condition, accurate to within $\pm 10\%$ in the range $4 < T_{max}^{no\,\alpha} < 8$, is given by

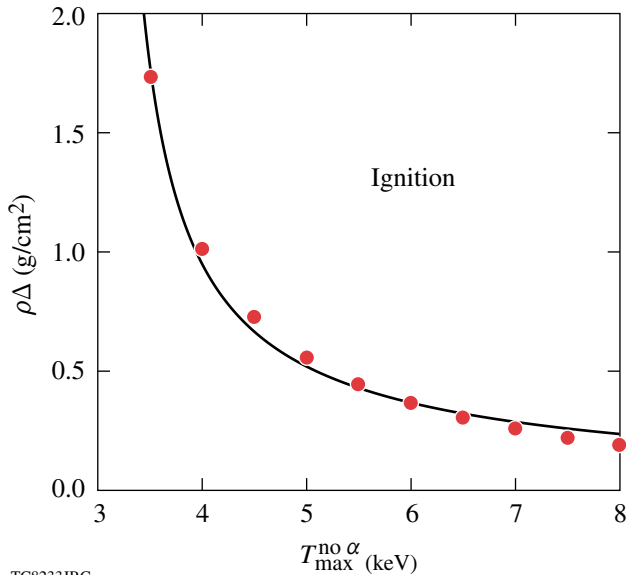$$(\rho\,\Delta) \approx \frac{2.5}{\left(T_{max}^{no\,\alpha}\right)^{1.18}\left[1 - \left(\dfrac{3}{T_{max}^{no\,\alpha}}\right)^{2.5}\right]} \,. \qquad (26)$$

The solid curve in Fig. 116.42 shows the numerical fit in relation to the exact numerical solution of the ignition model (dots). Notice that Eq. (26) exhibits a singularity for $T_{max}^{no\,\alpha} \approx 3$ keV, indicating that at such low temperatures, ignition requires very large areal densities. The areal density in Eq. (26) refers to the shell's areal density without including the hot spot's contribution. The hot spot's contribution to the areal density is typically small except for marginally ignited targets at high temperatures. As shown in Fig. 116.42, when the $T_{max}^{no\,\alpha}$ temperatures increase, the shell's areal density required for marginal ignition falls below 0.5 g/cm². At such low values, the areal densities of both the shell and the hot spot are of the same order and the hot spot's contribution is a significant portion of the total areal density. In the next section, the total areal density from a set of hydrodynamic simulations is used to generate an ignition

2.0

1.5

Ignition

1.0

0.5

0.0

$\rho\Delta$ (g/cm²)

3   4   5   6   7   8

$T_{max}^{no\,\alpha}$ (keV)

TC8233JRC

Figure 116.42

Relation between $\rho\Delta$ and $T_{max}^{no\,\alpha}$ according to the ignition model of Eq. (15). Each dot represents a single pair of $\rho\Delta$ and $T_{max}^{no\,\alpha}$ from the solution of Eqs. (24) and (25) for $4 < T_{max}^{no\,\alpha} < 8$. The solid curve is the fitting formula in Eq. (26) and represents the marginal ignition condition.

curve similar to the one in Fig. 116.42. Therefore, significant discrepancies between the theoretical and numerical results are expected at high ignition temperatures. A detailed discussion of the validity of Eq. (26) and a comparison with the results of numerical simulations are the subjects of the next section.

Hydrodynamic Simulations

About 20 marginally ignited direct-drive targets have been simulated with the one-dimensional Lagrangian radiation-hydrodynamic code *LILAC*.[21] *LILAC* is routinely used for ICF target design studies at the Laboratory for Laser Energetics. It includes *SESAME*[22] equation-of-state tables, flux-limited Spitzer thermal conduction (the value of the flux limiter is set at $f = 0.06$), multigroup radiation transport, multigroup alpha-particle transport, and 3-D laser ray tracing. The targets used in the simulations were spherical shells consisting of a single DT-ice layer or two layers of wetted-foam [(DT)$_6$CH] and pure-DT ice. All targets were filled with 1 atm of DT gas at 2.1×10^{-4} g/cm³, and the initial aspect ratio of the targets varied from 2.0 to 5.5. The relaxation (RX) adiabat shaping[23] technique was used to design most of the laser pulse shapes for these implosions. The relaxation (RX) laser pulse consisted of a prepulse followed by an interval of laser shut-off and the main pulse. Such a laser pulse is used to shape the adiabat in the ablator. In these simulations, the UV driver energy varies from 35 kJ to 10 MJ, adiabat from 0.7 to 4, and implosion velocity from 1.75 to 5.3×10^7 cm/s. These targets are designed to achieve marginal ignition with minimum laser energy. In the simulations, marginal ignition is defined as gain = 1 (fusion energy = laser energy on target). These implosions are also simulated without alpha energy deposition to compute the areal density and the no-alpha ion temperature used in the ignition condition (previous section).

Each dot in Figs. 116.43 and 116.44 shows the areal density and ion temperature of each marginally ignited target. Figure 116.43 shows the maximum total areal density and the maximum hot-spot-volume–averaged, no-alpha ion temperature (the volume average is carried out over the hot-spot volume). Observe that all the points lie on a curve (i.e., the ignition curve). The latter can be accurately approximated (Fig. 116.43) by the following fitting formula:

$$\rho R_{max} \approx \frac{33.5}{\left\langle T^{no\,\alpha}\right\rangle_v^{5/2}\left[1 - \left(\dfrac{1.2}{\left\langle T^{no\,\alpha}\right\rangle_v}\right)^{5/2}\right]^{4/3}} \,, \qquad (27)$$

where ρR_{max} is in g/cm² and $T^{no\,\alpha}$ is in keV. Similarly, Fig. 116.44 shows the ignition points in terms of the burn-
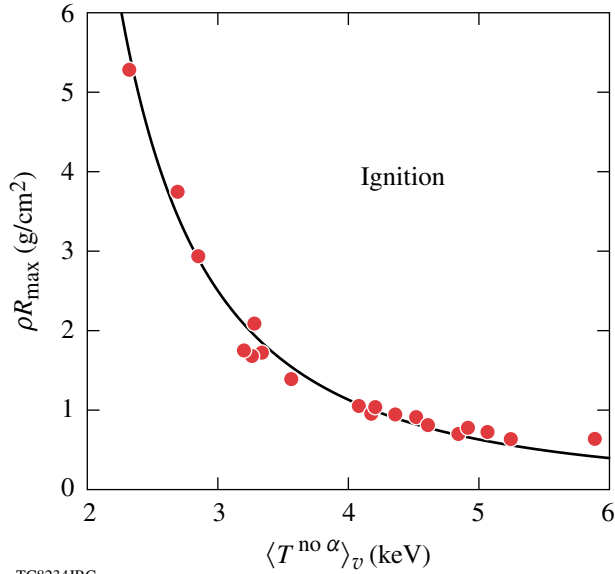
TC8234JRC

Figure 116.43
Relation between the maximum total areal density (ρR_{max}) and the maximum hot-spot volume-averaged, no-alpha ion temperature ($\langle T^{no\,\alpha} \rangle_v$) for marginally ignited targets. Each dot represents a single simulation from the 1-D hydrocode *LILAC*. The solid curve is the fitting formula in Eq. (27).
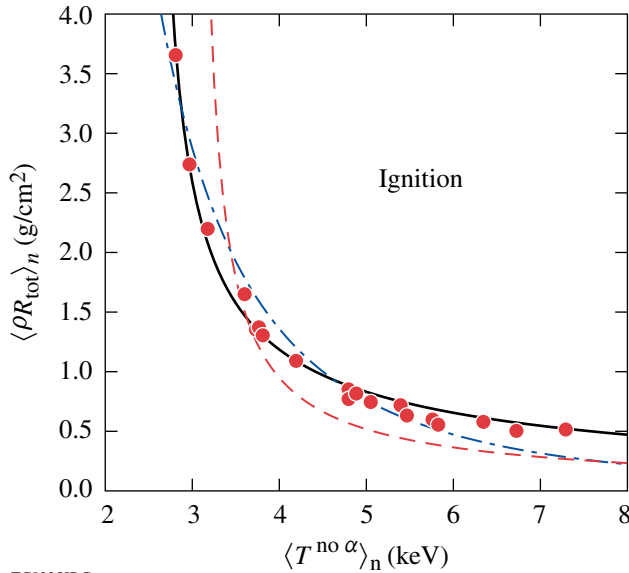

TC8235JRC

Figure 116.44
Relation between neutron-averaged, no-alpha temperature ($\langle T_i^{no\,\alpha} \rangle_n$) and neutron-averaged total areal density ($\langle \rho R_{tot} \rangle_n$) for marginally ignited targets. Each dot represents a single simulation from 1-D hydrocode. The solid curve is the fitting formula in Eq. (28). The dashed–dotted curve is the approximation of the ignition curve in Eq. (29). The dashed curve is the ignition model given in Eq. (26) of the **Solution of the Ignition Model and Marginal Ignition Condition** section (p. 209).

averaged areal density and the burn-averaged ion temperature. The burn-averaged areal density is defined as the total areal density weighted in time with the neutron rate. The burn-averaged temperature is the temperature weighted in time and space with the fusion reaction rate. Even in the $\langle \rho R_{tot} \rangle_n$, $\langle T_i^{no\,\alpha} \rangle_n$ plane the simulated marginal ignition points lie on an ignition curve. This curve is of particular importance since $\langle \rho R_{tot} \rangle_n$, $\langle T_i^{no\,\alpha} \rangle_n$ are the only two measurable parameters of the fuel assembly in an ICF implosion. The burn-averaged total areal density can be inferred from the downshift of the spectrum of charged fusion products,[13] and the burn-averaged ion temperature can be measured with the neutron time-of-flight diagnostics (nTOF's).[10] One can argue that the measurements give $\langle T_i \rangle_n$ instead of $\langle T_i^{no\,\alpha} \rangle_n$. The two parameters are virtually identical, however, for D_2 surrogate implosions or sub-ignited DT implosions with gain $\ll 1$. The ignition curve in Fig. 116.44 can also be approximated with a simple fitting formula

$$\langle \rho R_{tot} \rangle_n = \frac{3.4}{\langle T^{no\,\alpha} \rangle_n^{0.97} \left[1 - \left(\frac{2.5}{\langle T^{no\,\alpha} \rangle_n} \right)^{2.5} \right]^{0.79}}, \quad (28)$$

where $\langle \rho R_{tot} \rangle_n$ is in g/cm^2 and $\langle T^{no\,\alpha} \rangle_n$ is in keV. Equation (28), plotted as the solid curve in Fig. 116.44, is the most useful form of the ignition condition that can be directly measured. A rough approximation of the ignition curve can be cast into a simple power law

$$\langle \rho R_{tot} \rangle_n \times \langle T_i^{no\,\alpha} \rangle_n^{2.6} > 50 \text{ g} \times \text{cm}^{-2} \times \text{keV}^{2.6}. \quad (29)$$

The dashed–dotted line in Fig. 116.44 shows the simple fit [Eq. (29)] in relation to the simulation results (dots). To compare the ignition condition from the analytic model in the previous section with the simulation results, we plot Eq. (26) in the $\langle \rho R_{tot} \rangle_n$, $\langle T_i^{no\,\alpha} \rangle_n$ plan of Fig. 116.44. The dashed curve in Fig. 116.44 shows the ignition model results as given in Eq. (26). This suggests that in spite of its simplicity, the ignition model captures the essential physics and the ignition condition [Eq. (26)] is in reasonable agreement with the simulation results. Notice that, as expected, the model prediction (dashed curve) falls below the simulation results at high temperatures since the hot-spot areal density is not accounted for.

Alpha-Particle Confinement

An important assumption used in the analytic model in the **Solution of the Ignition Model and Marginal Ignition Condition** section (p. 209) concerns the alpha-particle confinement. The assumption was made that most of the alpha particles slow down within the hot spot, and that the alpha-particle energy

deposited inside the hot spot is close to 100% ($\theta \approx 1$). Since the alpha-energy deposition in the hot spot depends on its areal density and temperature,[24] we have computed the hot-spot areal densities and hot-spot temperature for the marginal ignited targets in our simulation database. Figure 116.45 shows the hot-spot areal density and temperature at marginal ignition from the 1-D simulations discussed in the previous section. Observe that all the marginally ignited targets have a hot-spot areal density above the critical value of 0.3 g/cm^2 often cited in the literature.[1,2] To estimate the fraction of absorbed alpha particles (θ), we use the results of Ref. 24 to find that

$$\theta = \frac{3\tau}{2} - \frac{4}{5}\tau^2, \tau \leq \frac{1}{2};$$

$$\theta = 1 - \frac{1}{4\tau} + \frac{1}{160\tau^2}, \tau \geq \frac{1}{2}; \qquad (30)$$

$$\tau \approx 92(\rho R)_{hs}\Big/T_h^{3/2},$$

where $(\rho R)_{hs}$ is the hot-spot areal density in g/cm^2 and T_h is the hot-spot temperature in keV. Substituting the areal densities and temperatures from Fig. 116.45 into Eq. (30) shows that the fraction of alpha energy deposited within the hot spot ranges from about 87% to 99% ($0.87 < \theta < 0.99$). Thus, our assumption that $\theta \approx 1$ seems to be satisfied at marginal ignition. It is also
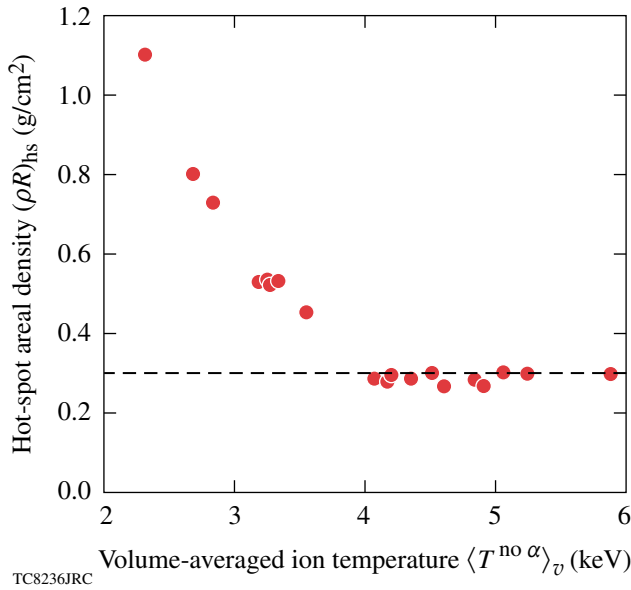

Figure 116.45
Hot-spot areal density $\left[(\rho R)_{hs}\right]$ and volume-averaged, no-alpha hot-spot ion temperature $\left(\langle T^{\text{no }\alpha}\rangle_v\right)$. Each dot represents a single simulation from 1-D hydrocode. The dashed line marks the hot-spot areal density of 0.3 g/cm^2.

interesting to observe that, as shown in Fig. 116.45, ignition at no-alpha temperatures $\langle T_h^{\text{no }\alpha}\rangle$ below 4 keV requires a hot-spot areal density well above the 0.3-g/cm^2 critical value.

For large hot-spot areal densities and low hot-spot temperatures, a significant fraction of the bremsstrahlung radiation and conductive heat flux is absorbed within the hot spot, thus preventing a severe temperature degradation. For these targets, the only confinement issue is with the hydrodynamic disassembly of the surrounding shells. Since high hot-spot areal densities are correlated with high shell areal densities,[9] the inertial confinement of such shells is very long and ignition can occur at very low no-alpha temperatures, as shown in Fig. 116.45.

Comparison with the HTL Ignition Condition
To test the validity of the ignition condition derived in this article, we compare it to the ignition criterion derived by Herrmann *et al.* in Ref. 25. We refer to the criterion of Ref. 25 as the Herrmann–Tabak–Lindl (HTL) ignition condition. The HTL condition is a more accurate extension of the ignition scaling of Levedahl and Lindl,[26] and it correlates the minimum shell kinetic energy required for ignition with the implosion velocity, shell adiabat, and ablation pressure. Since all our simulations are for direct-drive targets with maximum intensity around 10^{15} W/cm^2, we will use the form of the HTL condition rewritten in terms of laser energy on target rather than the shell kinetic energy as shown in Eq. (53) of Ref. 9. The relation between laser energy and kinetic energy is $E_L = E_\kappa/\eta$, where η is the overall hydrodynamic efficiency. For intensities of 10^{15} W/cm^2, our 1-D hydrodynamic simulations show an ablation pressure close to 200 Mbar at the end of the acceleration phase in spherical implosions. Using $I_{15} = 1$ and $P_L = 200$ Mbar into Eq. (53) of Ref. 9, we find the following modified HTL ignition criterion:

$$E_L \approx 5.9 \times 10^2 \alpha_{if}^{1.9}\left(\frac{3 \times 10^7}{V_i}\right)^{6.6}, \qquad (31)$$

where the laser energy E_L is in kJ and the implosion velocity V_i in cm/s. Since our ignition criterion uses the areal density and the ion temperature, a relation between these variables and those in Eq. (31) is required. For simplicity, we will consider the simplest (and the least accurate) form of our criterion, $\langle T^{\text{no }\alpha}\rangle_n^{2.6} \times \langle \rho R\rangle_n > 50$ keV$^{2.6} \times$ g/cm^2. The scaling relations derived in Ref. 9 provide accurate formulas relating the maximum areal density and the maximum volume-averaged, no-alpha temperature to the laser energy, shell adiabat, and implosion velocity. We will use the same scaling relation in Ref. 9 and simply adjust the proportionality constant to fit the neutron-averaged quantities in our ignition criterion. A simple fit of the numerical results from our implosion database leads to

TC8236JRC

$$\langle \rho R \rangle_n (E_L) = \frac{0.78}{\alpha_{if}^{0.54}} \left(\frac{V_i}{3 \times 10^7} \right)^{0.06} \left(\frac{E_L}{100} \right)^{0.33}$$

$$\langle T_i^{no\,\alpha} \rangle_n (E_L) = \frac{3.5}{\alpha_{if}^{0.15}} \left(\frac{V_i}{3 \times 10^7} \right)^{1.25} \left(\frac{E_L}{100} \right)^{0.07}. \qquad (32)$$

Figures 116.46 and 116.47 compare the results of the simulations with the above fitting formulas. Substituting Eq. (32) into our ignition criterion yields the minimum energy required for

$$E_L\,(\text{kJ}) > 5.9 \times 10^2 \alpha_{if}^{1.8} \left(\frac{3 \times 10^7}{V_i} \right)^{6.5}. \qquad (33)$$

Notice that the power indices and the proportionality constants in Eq. (33) are virtually identical to those in Eq. (31). This shows that our ignition criterion reproduces the HTL scaling quite accurately.
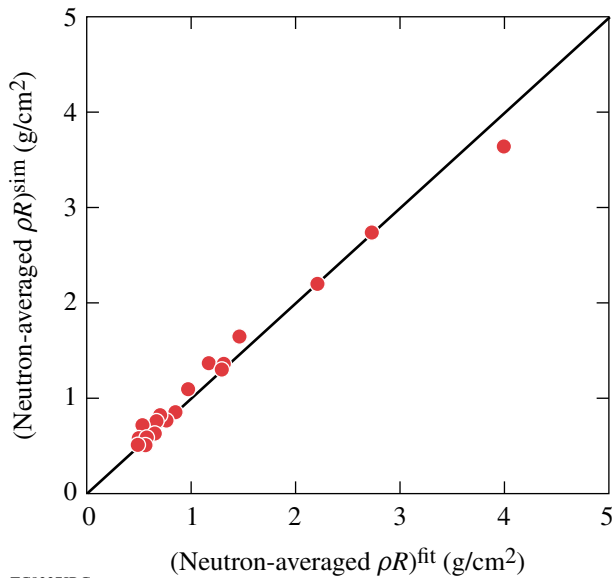

TC8237JRC

Figure 116.46
Neutron-averaged areal density $\langle \rho R \rangle_n$ from simulations (dots) compared to the numerical fit in Eq. (32) (solid line).

Hydro-Equivalent Curves

In this section we introduce the concept of hydro-equivalency and hyro-equivalent curves in the ρR, T_i plane. ICF targets with similar in-flight hydrodynamic variables, but different driver energy and gain, are considered hydrodynamically equivalent. Hydro-equivalent targets are expected to exhibit the same hydrodynamic behavior with respect to their hydro-
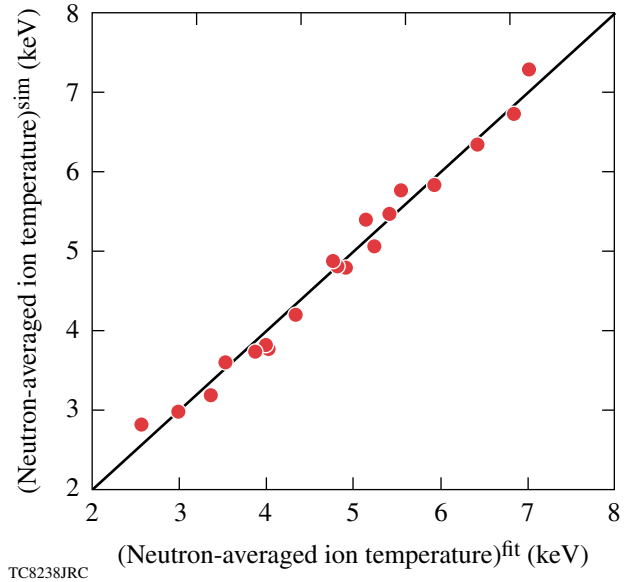

TC8238JRC

Figure 116.47
Neutron-averaged, no-alpha ion temperature $\langle T_i^{no\,\alpha} \rangle_n$ from simulation (dots) compared to the numerical fit in Eq. (32) (solid line).

dynamic performance not only in 1-D but also in 3-D. Here, we relate the hydrodynamic performance to the peak pressure of the stagnating core and to the hydrodynamic stability of the implosion. If a set of targets is scaled in mass (M), radius (R), thickness (Δ), adiabat (α), implosion velocity (V_i), laser intensity (I), and energy (E_L) according to the simple scaling $M \sim E_L$, $R \sim E_L^{1/3}$, $\Delta + E_L^{1/3}$, $I \sim$ constant, $\alpha \sim$ constant, and $V_i \sim$ constant, then the target implosions yield the same peak pressure and the same hydrodynamic stability properties. The latter is related to the magnitude of the in-flight aspect ratio (IFAR), which depends on the implosion velocity, adiabat, and laser intensity (Ref. 9). Assuming the same relative size of the initial perturbations on targets, hydro-equivalent targets have the same Rayleigh–Taylor (RT) growth factor (Ref. 9) and the same RT amplitude with respect to their thicknesses. As shown in Eqs. (32) (and in Ref. 9), due to the dependence on the laser energy E_L, hydro-equivalent targets will produce different areal densities and slightly different no-alpha temperatures. Obviously, targets imploded by larger drivers (larger E_L) will achieve greater ρR and T_i.

Using Eqs. (32), one can easily plot hydro-equivalent curves on the $\langle \rho R \rangle_n$, $\langle T^{no\,\alpha} \rangle_n$ ignition plane, by fixing α and V_i in Eqs. (32) and letting E_L vary. In Fig. 116.48, we plot two hydro-equivalent curves for the direct-drive NIF point design[27] and the current best-performing cryogenic D_2 implosion on OMEGA to date.[11] The direct-drive NIF point design
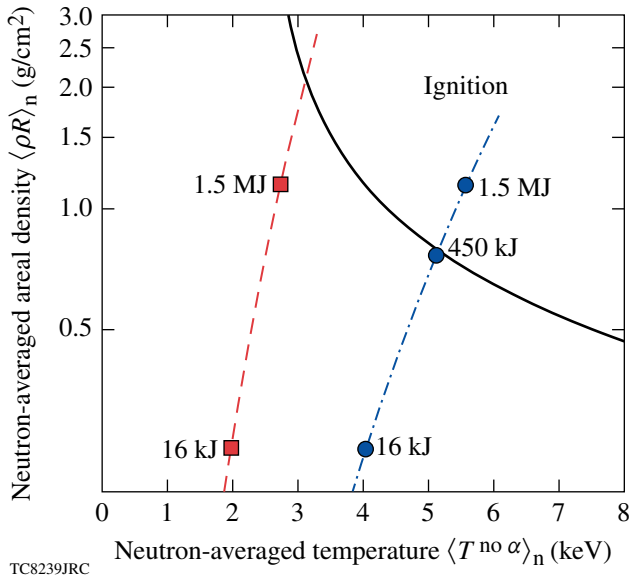
TC8239JRC

Figure 116.48

Hydro-equivalent curves in the $\left(\langle\rho R\rangle_{\mathrm{n}}, \langle T^{\mathrm{no}\,\alpha}\rangle_{\mathrm{n}}\right)$ plane. The solid curve is the ignition condition in Eq. (28). The dashed curve is the hydro-equivalent curve for implosions with $\alpha_{\mathrm{if}} = 2.5$, $V_i = 2.4 \times 10^7$ cm/s in Eq. (32). The lower square represents an implosion at 16 kJ and the upper one at 1.5 MJ. The dashed–dotted curve is the hydro-equivalent curve for implosions with $\alpha_{\mathrm{if}} = 2.7$, $V_i = 4.25 \times 10^7$ cm/s. The three dots are implosions at 16 kJ, 450 kJ, and 1.5 MJ, respectively.

has an in-flight adiabat of 2.7 and implosion velocity of 4.25×10^7 cm/s. The hydro-equivalent curve for such values of α_{if} and V_i is the dashed–dotted curve in Fig. 116.48. The bottom dot on such a curve is the hydro-equivalent point for a 16-kJ implosion. The areal density and no-alpha temperature corresponding to that point are $\langle\rho R\rangle_{\mathrm{n}} \approx 0.25$ g/cm² and $\langle T^{\mathrm{no}\,\alpha}\rangle_{\mathrm{n}} \approx 4.1$ keV, respectively. The top dot on the same curve represents the same implosion scaled up to NIF-like energies of 1.5 MJ. The middle dot is the same implosion scaled up to 450 kJ. Notice that the 450-kJ implosion is right on the 1-D marginal ignition curve (the solid curve in Fig. 116.48). This shows that the full NIF energy of 1.5 MJ is approximately three times larger than required for 1-D marginal ignition. The plots in Fig. 116.48 mainly imply that if a 16-kJ cryogenic implosion is carried out on OMEGA to achieve areal densities and temperatures as indicated on the bottom point, then one can use such a result to theoretically conclude that the same implosion scaled up to the NIF will have three times more energy as required by the 1-D Lawson criterion. While this is not absolute proof that such a target will ignite on the NIF, it will establish some confidence in the achievement of ignition.

The point representing the highest areal density cryogenic implosion on the OMEGA laser to date is the bottom square on the dashed curve. The point represents a neutron-averaged areal density slightly exceeding 0.2 g/cm² and neutron-averaged temperature of 2 keV. The corresponding implosion had an in-flight adiabat of about 2.5 and implosion velocity of about 2.4×10^7 cm/s. The upper square on that hydro-equivalent curve is below the marginal ignition curves and represents the same implosion scaled up to the full NIF energy of 1.5 MJ. Obviously, such an implosion would fail to ignite. This is explained by the relatively low implosion velocity ($V_i \approx 2.4 \times 10^7$ cm/s) and by the sensitivity on V_i of the minimum energy required for ignition [see Eq. (33)]. Current OMEGA cryogenic targets are massive shells (430-μm outer diam) with a 95-μm-thick cryogenic layer and a 10-μm-thick plastic ablator used to study high compression while reducing the effect of hydrodynamic instabilities. A point worth making is that current OMEGA targets have been imploded with ignition-relevant adiabats that are even slightly below the value required for the direct-drive point design.

In summary, hydro-equivalent curves plotted on the ρR, T_i ignition plane are useful in predicting 1-D performance for different laser energies. An immediate conclusion is that OMEGA-size capsules will have to be imploded at higher implosion velocities (for the same adiabat) to achieve a hydro-equivalent demonstration of ignition.

Conclusions

Equation (28) provides an accurate representation of a measurable Lawson criterion for inertial confinement fusion with DT fuel. Such an ignition condition is found using an analytical dynamic model of ignition, and it is confirmed by the results of one-dimensional simulations of marginally ignited direct-drive targets (gain $\approx$ 1). A simple fit of the ignition condition can be written as

$$\left\langle T_i^{\mathrm{no}\,\alpha}\right\rangle_{\mathrm{n}}^{2.6} \times \langle\rho R_{\mathrm{tot}}\rangle_{\mathrm{n}} > 50 \text{ keV}^{2.6} \times \mathrm{g}/\mathrm{cm}^2. \qquad (34)$$

This ignition condition is given in terms of the only two measurable parameters of the compressed fuel: (1) the burn-averaged total areal density $\langle\rho R_{\mathrm{tot}}\rangle_{\mathrm{n}}$, and (2) the neutron-averaged hot-spot ion temperature $\langle T_i^{\mathrm{no}\,\alpha}\rangle_{\mathrm{n}}$ without accounting for the α-particle energy deposition. The burn-averaged total areal density can be measured through the detection of the spectrum of fusion products such as protons from secondary reactions.[13] The neutron-averaged temperature is measured through the neutron time-of-flight diagnostic.[10] In our ignition

condition, the neutron-averaged ion temperature is computed without the contribution of the fusion alpha particles. This is done to avoid using the actual temperature that undergoes extremely large and sudden variations when the compressed fuel assembly approaches the ignition condition. The so-called no-alpha temperature $T^{no\,\alpha}$ used in this article is a slowly varying hydrodynamic parameter that is well suited to measure the implosion performance with respect to the ignition condition. The only drawback for using $T^{no\,\alpha}$ rather than T is that $T^{no\,\alpha}$ is not always equal to the actual measurable temperature. The no-alpha temperature and the real temperature are virtually identical for cryogenic implosions with surrogate fuel (such as D_2) and for sub-ignited DT implosions with gains much less than unity. In both cases, the fusion self-heating is negligible and $T^{no\,\alpha} \approx T$. For DT implosions approaching ignition (gains ≥ 0.1), the alpha heating plays an important role in determining the hot-spot temperature and our form of the Lawson criterion cannot be used. In this case, however, the neutron-yield measurement alone is sufficient to determine that the implosion is approaching ignition. Because of the large excursion in neutron yield of a target approaching ignition (commonly referred to as the "ignition cliff"), the neutron yield rather than a formula like Eq. (34) is a much better indicator of target performance.

The measurable Lawson criterion, Eq. (34), favorably compares with the Herrmann–Tabak–Lindl ignition scaling when the areal density and temperature are rewritten in terms of the implosion velocity, in-flight adiabat, and driver energy by using the conversion formulas Eqs. (32) (also from Ref. 9). Furthermore, hydro-equivalent curves [Eqs. (32)] are plotted on the ignition diagram to show how hydro-equivalent implosions would perform with respect to the ignition condition when scaled up in laser energy.

It is worth mentioning that the ignition model presented here could be modified according to the results in Ref. 28 to include the effects of hydrodynamic instabilities developing at the hot-spot/shell interfaces. Such an extension of the ignition model could lead to a more accurate ignition condition that is valid in multidimensions.

REFERENCES

1. S. Atzeni and J. Meyer-ter-Vehn, *The Physics of Inertial Fusion: Beam Plasma Interaction, Hydrodynamics, Hot Dense Matter*, International Series of Monographs on Physics (Clarendon Press, Oxford, 2004).

2. J. D. Lindl, *Inertial Confinement Fusion: The Quest for Ignition and Energy Gain Using Indirect Drive* (Springer-Verlag, New York, 1998).

3. J. D. Lawson, Proc. Phys. Soc. Lond. **B70**, 6 (1957).

4. S. Atzeni and A. Caruso, Phys. Lett. A **85**, 345 (1981).

5. S. Yu. Gus'kov, O. N. Krokhin, and V. B. Rozanov, Nucl. Fusion **16**, 957 (1976).

6. R. Kishony, E. Waxman, and D. Shvarts, Phys. Plasmas **4**, 1385 (1997).

7. R. Betti, M. Umansky, V. Lobatchev, V. N. Goncharov, and R. L. McCrory, Phys. Plasmas **8**, 5257 (2001).

8. R. Betti, K. Anderson, V. N. Goncharov, R. L. McCrory, D. D. Meyerhofer, S. Skupsky, and R. P. J. Town, Phys. Plasmas **9**, 2277 (2002).

9. C. D. Zhou and R. Betti, Phys. Plasmas **14**, 072703 (2007).

10. V. Yu. Glebov, D. D. Meyerhofer, C. Stoeckl, and J. D. Zuegel, Rev. Sci. Instrum. **72**, 824 (2001).

11. T. C. Sangster, V. N. Goncharov, P. B. Radha, V. A. Smalyuk, R. Betti, R. S. Craxton, J. A. Delettrez, D. H. Edgell, V. Yu. Glebov, D. R. Harding, D. Jacobs-Perkins, J. P. Knauer, F. J. Marshall, R. L. McCrory, P. W. McKenty, D. D. Meyerhofer, S. P. Regan, W. Seka, R. W. Short, S. Skupsky, J. M. Soures, C. Stoeckl, B. Yaakobi, D. Shvarts, J. A. Frenje, C. K. Li, R. D. Petrasso, and F. H. Séguin, Phys. Rev. Lett. **100**, 185006 (2008).

12. T. R. Boehly, D. L. Brown, R. S. Craxton, R. L. Keck, J. P. Knauer, J. H. Kelly, T. J. Kessler, S. A. Kumpan, S. J. Loucks, S. A. Letzring, F. J. Marshall, R. L. McCrory, S. F. B. Morse, W. Seka, J. M. Soures, and C. P. Verdon, Opt. Commun. **133**, 495 (1997).

13. J. A. Frenje, C. K. Li, F. H. Séguin, J. Deciantis, S. Kurebayashi, J. R. Rygg, R. D. Petrasso, J. Delettrez, V. Yu. Glebov, C. Stoeckl, F. J. Marshall, D. D. Meyerhofer, T. C. Sangster, V. A. Smalyuk, and J. M. Soures, Phys. Plasmas **11**, 2798 (2003).

14. E. M. Campbell and W. J. Hogan, Plasma Phys. Control. Fusion **41**, B39 (1999).

15. D. Mihalas and B. Weibel-Mihalas, *Foundations of Radiation Hydrodynamics* (Oxford University Press, New York, 1984).

16. Ya. B. Zel'dovich and Yu. P. Raizer, in *Physics of Shock Waves and High-Temperature Hydrodynamic Phenomena*, edited by W. D. Hayes and R. F. Probstein (Dover Publications, Mineola, NY, 2002).

17. S. Atzeni and A. Caruso, Nuovo Cimento B **80**, 71 (1984).

18. H.-S. Bosch and G. M. Hale, Nucl. Fusion **32**, 611 (1992).

19. Y. Saillard, Nucl. Fusion **46**, 1017 (2006).

20. R. Betti and C. Zhou, Phys. Plasmas **12**, 110702 (2005).

21. M. C. Richardson, P. W. McKenty, F. J. Marshall, C. P. Verdon, J. M. Soures, R. L. McCrory, O. Barnouin, R. S. Craxton, J. Delettrez, R. L. Hutchison, P. A. Jaanimagi, R. Keck, T. Kessler, H. Kim, S. A. Letzring, D. M. Roback, W. Seka, S. Skupsky, B. Yaakobi, S. M. Lane, and S. Prussin, in *Laser Interaction and Related Plasma Phenomena*, edited by H. Hora and G. H. Miley (Plenum Publishing, New York, 1986), Vol. 7, pp. 421–448.

22. S. P. Lyon and J. D. Johnson, Los Alamos National Laboratory, Los Alamos, NM, Report LA-UR-92-3407 (1992).

23. K. Anderson and R. Betti, Phys. Plasmas **11**, 5 (2004).

24. O. N. Krokhin and V. B. Rozanov, Sov. J. Quantum Electron. **2**, 393 (1973).

25. M. C. Herrmann, M. Tabak, and J. D. Lindl, Nucl. Fusion **41**, 99 (2001).

26. W. K. Levedahl and J. D. Lindl, Nucl. Fusion **37**, 165 (1997).

27. P. W. McKenty, V. N. Goncharov, R. P. J. Town, S. Skupsky, R. Betti, and R. L. McCrory, Phys. Plasmas **8**, 2315 (2001).

28. J. Sanz *et al.*, Phys. Plasmas **12**, 112702 (2005).